

Research Article

Seismic Performance of Damaged Dovetail Joints with Different Damaged Degrees in Timber Frames

Hua Ma ¹, Xinyu Luan ¹, Zhenbao Li ¹, Haijian Cui,¹ Wenjing Wang,^{1,2,3,4} and Jia Song⁵

¹The Key Laboratory of Urban Security and Disaster Engineering, Ministry of Education, Beijing University of Technology, Beijing 100124, China

²China State Construction Development Co., Ltd., Beijing 100037, China

³China Construction Science & Technology Co., Ltd., Beijing 100070, China

⁴China State Construction Engineering Corporation (CSCEC), Beijing 100029, China

⁵China Construction Prefabricated Building Design & Research Institute Co., Ltd., Beijing 100070, China

Correspondence should be addressed to Zhenbao Li; lizb@bjut.edu.cn

Received 29 April 2019; Revised 27 June 2019; Accepted 25 July 2019; Published 21 August 2019

Academic Editor: Giulio Castori

Copyright © 2019 Hua Ma et al. This is an open access article distributed under the Creative Commons Attribution License, which permits unrestricted use, distribution, and reproduction in any medium, provided the original work is properly cited.

The mortise and tenon joints are the main connection forms used in ancient timber buildings, and damaged joints have a critical effect on the safety of a timber structure. There are three main damaged cases of dovetail joints which are pulling, contraction, and mixing damages. In this study, using a theoretical analysis of the stress distribution in a mortise and tenon joint resulted from the pullout damage, a theoretical equation for the resisting moment of the joint was proposed. A finite element model was used to simulate the cyclic displacement loading of a frame with intact joints and with different levels of pulling and contraction damaged joints. The results show that the moment capacities both for the test and the simulation were in good agreement with each other. The simulation results also indicated that there are no changes in the capacity and energy dissipation of the pulling damaged joint compared to that of the intact joint, and good seismic performance still was provided when the pulling damage was less than 2/5 of the joint length. However, the capacity of the contraction damaged joint was significantly reduced, and its seismic performance was tolerably lost. The seismic performance of a mixing damaged tenon with the same degree of pulling damage was between that of the pulling damaged tenon and the contraction damaged tenon, and generally, it was controlled by the contraction damage. The friction between the tenon and the mortise is the main source of resisting moment and energy dissipation ability.

1. Introduction

Timber structures have been used widely around the world throughout the history, including China, Japan, Korea, Canada, the USA, and northern Europe [1, 2]. These connections mainly include the straight tenon joints (Figure 1(a)) and the dovetail joints (Figure 1(b)). The mortise and tenon connections are the most important connections in ancient timber structures and have been demonstrated to exhibit semirigid characteristics [3–8]. These characteristics have typically been exhibited through lateral loading tests of timber frames incorporating mortise and tenon joints [9–13], in which a vertical load is applied to the top of the columns to simulate a gravity load, and a lateral cyclic load is applied by a horizontal actuator using

displacement control. In these tests, the hysteresis curves obtained have been relatively full, and the joints have displayed good deformation and energy dissipation ability. Generally, the failure mode of mortise and tenon joints has been found to be the pullout failure of the tenon [11–13].

Research on mortise and tenon connections has typically focused on intact joints. Zhao et al. [14] and Dong et al. [15] proposed the variable rigidity unit and the two node-space virtual spring element, respectively, to simulate mortise and tenon joints. Wu et al. [16] subjected a typical dovetail joint model to low-cycle cyclic loading to evaluate the behaviors of the semirigid connection and its stiffness degeneration properties. Zhou et al. [17] analyzed the seismic performance of a four-column, four-beam model based on the frame of a hall in the Forbidden City under low-cycle cyclic loading,

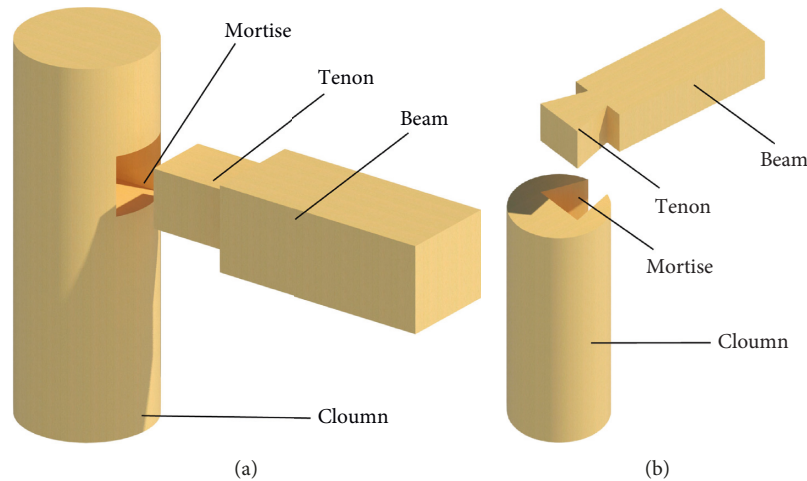


FIGURE 1: Joints in Chinese ancient timber building. (a) Straight tenon joint and (b) dovetail joint.

and they found that the bending moment-hysteresis curve of the model at the joints exhibited noticeable characteristics of pinching and closing, and the skeleton curve exhibited a smooth rotation angle and obtained the good ductility characteristics. Xie et al. [18] derived a theoretical equation for the bending moment and rotation angle of a dovetail joint based on the force transfer mechanism of the joint and analyzed the factors affecting the bending moment in the joint. Seo et al. [19] conducted a similar study of typical joints in the ancient Korean residential architecture. They used static and cyclic loading tests on a prototype frame model and resulted in a trilinear model of the hysteresis curve of displacement and load. The optimal angle and length of the wooden wedge (in Japanese, so called Nuki joint) were determined by Kato and Komatsu [20] by studying the extension length and working mechanism. Leichti et al. [4] evaluated several factors which affected the stiffness of a Nuki joint. They used the data obtained from the existing literature and conducted the numerical analysis study to observe the revolution of joint stiffnesses. According to their work, they divided the joints into three types which are fixed, semirigid, and rigid phases. Guan et al. [21] conducted experiments and numerical simulations on the behavior of a timber wedge in a Japanese Nuki joint. They found that the process of inserting the timber wedge led the increase of the initial stress and strain and initial stiffness of the joint. They also observed that the timber wedge increases the pullout resistance of the joint.

In this field, there has been little research on the performance of damaged dovetail joints, and most damaged characteristics have been mainly determined by the numerical method. Pang et al. [22] investigated the influence of the condition of the beam shoulder on the moment bearing capacity of a mortise and tenon joint using static load tests. The moment resistance and failure mode indicated that the condition of the beam shoulder significantly affected the performance of the joint. Wu et al. [23] evaluated tenon pulling damage by conducting a vertical load test of a mortise and tenon joint using four groups of typical single dovetail joint frame models to obtain the elastic modulus

and the variation in stiffness under both static load and applied deflection. Li [24] adopted a method of reducing the tenon head size to simulate loosening in joint models and then proposed a double-parameter damage assessment model based on the degree of loosening by studying the resulting behavior. The influence of the $P-\Delta$ effect on the behavior of timber frames connected by dovetailed (ITSD) mortise and tenon joints was discussed in detail by Li et al. [13]. Chen et al. [25] proposed a simplified mechanics model for the relationship between moment and rotation in dovetailed mortise-tenon joints. The failure modes were studied under monotonic loading, and numerical simulations were performed to confirm the observed deformation and stress distribution.

In recent years, some achievements about traditional timber frames and mortise and tenon joints have been obtained. Xie et al. [26] proposed a friction constitutive model for the friction behavior between mortise and tenon based on the modern frictional theory. Wen et al. [27] analyzed the wood frame structure and found the friction sliding of mortise-tenon joints has better seismic reduction effect under earthquake.

The behavior of damaged dovetail joints conducive to improve the conservation and restoration of ancient timber structures require a theoretical method to determine the likely performance of the joint-containing structure under seismic loading. In order to theoretically derive a method for calculating the resisting moment of a joint, in this paper, the effects of damage caused by an external force (pulling damage), the shrinkage of the tenon (contraction damage), or a combination of the two are determined. The effects of these types of damages are simulated by performing a pseudostatic numerical simulation of a dovetail truss subjected to different deflection angles and loads. By comparing the results of the theoretical and numerical analyses, the changes in the seismic performance of the joints after damage can be illustrated, assisting conservation efforts by improving the ability of restoration workers to evaluate the condition of ancient timber structures.

2. Theoretical Calculation of Joint Bending Moment

An earthquake subjects a timber frame to a horizontal cyclic action, causing the joints to rotate, analogous to the reciprocal loading of a frame during a lab simulation, during which the overall deflected shape of the frame can be divided into five positions: normal (unloaded), upward loading, upward unloading, downward loading, and downward unloading. Typically, the frame shape under loading and unloading can be considered the same when the column is at the same displacement. Figure 2 shows the behavior of the mortise and tenon joints when subjected to the different rotation states caused by reciprocal loading.

After rotating to a certain limit, the joint will resist the applied moment, restricting the rotation of the joint. For an intact joint, the contact between the tenon and the mortise becomes local contact at this time, consisting of an extraction force created by the moment and a corresponding friction force between the mortise and tenon in the resulting compression zone at the points of contact. These extraction, compression, and friction forces are shown in Figure 3.

The following assumptions have been made in the derivation of the bending moment calculation formula: (1) when determining the displacement at each point on the tenon, the tenon is assumed to move as a rigid body within the mortise; (2) the effect of the upper and lower faces of the mortise are the same, and the compression embedment region is considered to deform along the width of the tenon; (3) the stress-strain relationship of the timber strip compression and the straight-grain compression is in line with the simplified bifurcation model; (4) in the elastic stage, the compressive stress in the contact area is proportional to the deformation due to deflection. When subjected to upward loading, the deformation area of the tenon head can be described as shown in Figure 4, in which the contact areas of the top, bottom, and front surfaces of the tenon head are represented by t , d , and f , respectively.

The geometric parameters of the compression zone deformation at t are given by

$$\begin{aligned}\delta_t &= \frac{h_s/2}{\cos \theta} - \frac{h_s}{2}, \\ x_t &= \frac{h_s}{2} \left(\frac{1}{\sin \theta} - \frac{\cos \theta}{\sin \theta} \right), \\ m_t &= \delta_t.\end{aligned}\quad (1)$$

The geometric parameters of the compression zone deformation at f are given by

$$\begin{aligned}\delta_f &= L_s \cos \theta + \frac{h_s}{2} \sin \theta - L_s - \delta_0 \cos \theta, \\ x_f &= L_s \sin \theta - \left(\frac{h_s}{2} \cos \theta + \delta_0 \sin \theta - \frac{h_s}{2} \right), \\ m_f &= \frac{\delta_f}{\tan \theta} + \delta_f \tan \theta.\end{aligned}\quad (2)$$

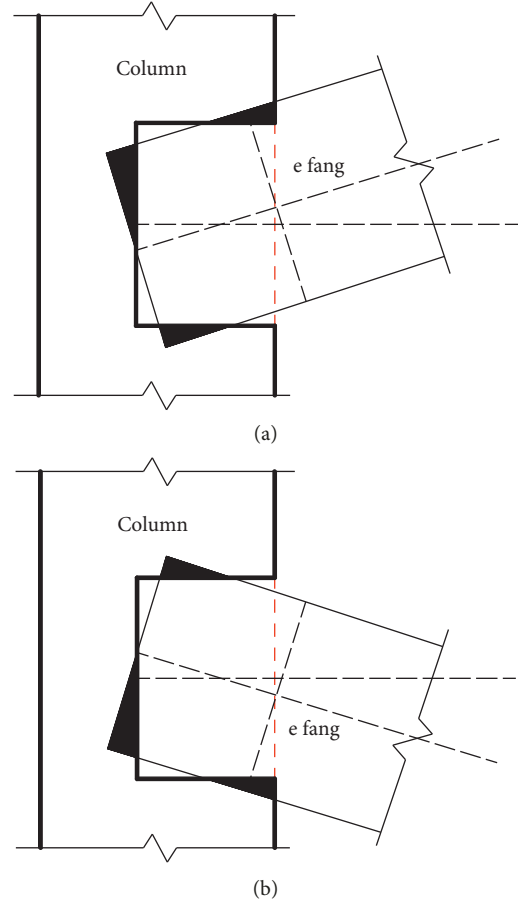


FIGURE 2: Horizontal displacement loading directions. (a) Upward loading and unloading and (b) downward loading and unloading.

The geometric parameters of the compression zone deformation at d are given by

$$\begin{aligned}\delta_d &= \frac{h_s/2}{\cos \theta} - \frac{h_s}{2} + x_d \tan \theta, \\ x_d &= \left(L_s - \frac{h_s}{2} \tan \theta \right) - \delta_0 \cos \theta, \\ m_d &= x_d + \delta_d \tan \theta,\end{aligned}\quad (3)$$

where the maximum deformation in each compression zone is indicated by δ_t , δ_f , and δ_d ; the length of each compression zone is indicated by m_t , m_f , and m_d ; the maximum deflected position of each point is indicated by x_t , x_f , and x_d ; the length of the tenon is L_s ; the height of the tenon is h_s ; θ is the rotation angle of the joint; δ_0 is the extracted displacement of the tenon from the mortise, measured between the midheight of the mortise and the center of the cross section of the tenon neck (Figure 5). The bending moment in the joint is calculated at the same location as δ_0 is measured: at the centroid of the cross section of the tenon neck.

The method for solving the extracted displacement of the tenon δ_0 is as follows:

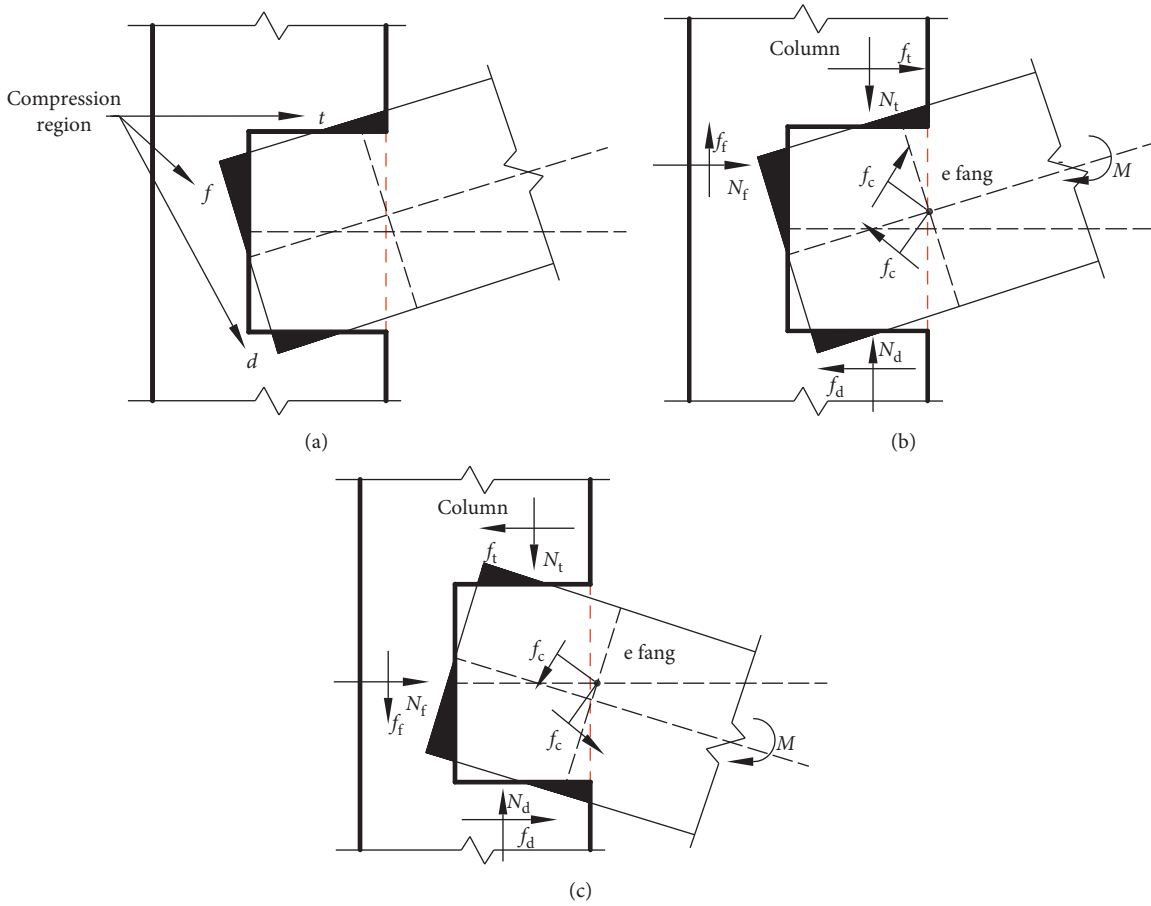


FIGURE 3: Forces on mortise and tenon joints under horizontal displacement of frame: (a) tenon compression zones, (b) upward loading, and (c) downward loading.

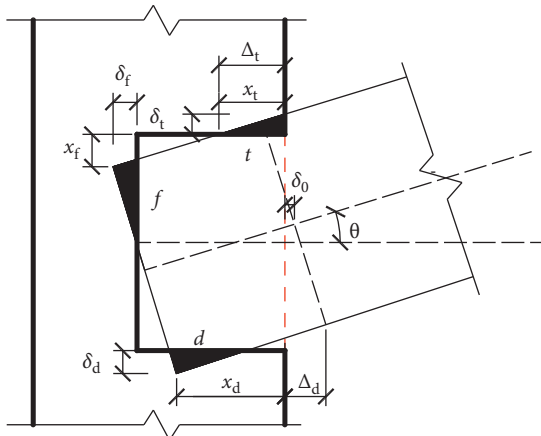


FIGURE 4: Tenon deflection under upward loading.

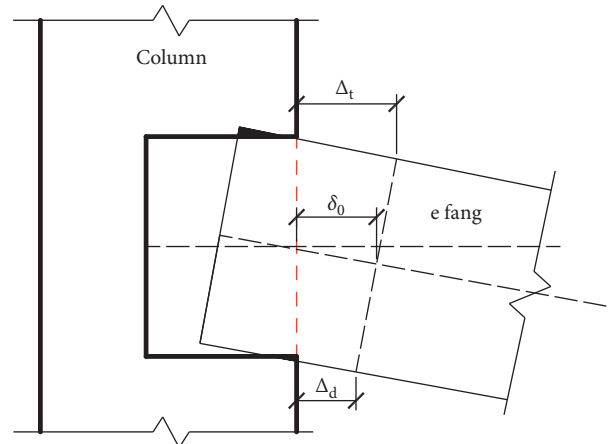


FIGURE 5: Tenon deflection under downward loading.

$$\delta_0 = \frac{\Delta_u + \Delta_t}{2} + \delta_e, \quad (4)$$

where Δ_u and Δ_t are the extracted displacements at the upper and lower faces of the tenon, respectively, and δ_e accounts for the amount of initial displacement due to damage.

Regardless of the direction of loading or unloading, the extraction deformation state is the same, so whether

evaluating the upward or downward direction, the geometric extraction deformation equations change only by exchanging the t zone and the d zone. After obtaining the deformation of the compression zone, the compression force and its corresponding friction force can be solved according to the physical conditions present. When the calculated maximum compression stress is less than or equal to the yield strength of the timber, the entire compression zone is

in the elastic stage; when the maximum compression stress is greater than the yield strength of the timber, a part of the compression zone enters the plastic stage. At this time, the deformations corresponding to the ultimate compressive strengths of the crushed zones t , d , and f are indicated by δ_{t1} , δ_{f1} , and δ_{d1} respectively, and the length of the elastic and plastic zones in t , d , and f is indicated by m_{t1} , m_{d1} , and m_{f1} and m_{t2} , m_{d2} , and m_{f2} , respectively, as shown in Figure 6.

In the elastic stage, the compressive forces are given by

$$N_t = \frac{1}{2}m_t b_s k_t \delta_t, \quad (5)$$

$$N_f = \frac{1}{2}m_f b_s k_f \delta_f, \quad (5)$$

$$N_d = \frac{1}{2}m_d b_s k_d \delta_d,$$

and the locations of the compression forces are given by

$$y_{f1} = \frac{1}{3}x_f, \quad (6)$$

$$y_{t1} = \frac{2}{3}x_t, \quad (6)$$

$$y_{d1} = \frac{h_s}{2} - \left(x_d + \frac{m_d}{3}\right).$$

For the elastoplastic stage, the compression force is given by

$$N_{t1} = \frac{1}{2}m_{t1} b_s f_{c,90}, \quad (7)$$

for the plastic zone, the compression force is given by

$$N_{t1} = m_{t1} b_s f_{c,90}. \quad (8)$$

Thus, the t region compression force is as follows:

$$N_t = N_{f1} + N_{f2} = \frac{1}{2}b_s f_{c,90} (m_{t1} + 2m_{t2}), \quad (9)$$

the f region compression force is

$$N_f = N_{f1} + N_{f2} = \frac{1}{2}b_s f_{c,90} (m_{f1} + 2m_{f2}), \quad (10)$$

the d region compression force is

$$N_d = N_{d1} + N_{d2} = \frac{1}{2}b_s f_{c,90} (m_{d1} + 2m_{d2}), \quad (11)$$

and the locations of the forces are given by

$$y_{t1} = \frac{1 - (1/3)(f_{c,90}/k_t \delta_t)^2}{2 - (f_{c,90}/k_t \delta_t)} m_t, \quad (12)$$

$$y_{f1} = \frac{(1/3)(f_{c,90}/k_f \delta_f)^2 - (f_{c,90}/k_f \delta_f) + 1}{2 - (f_{c,90}/k_f \delta_f)} m_f,$$

$$y_{d1} = \frac{h_s}{2} - x_d - \frac{(1/9)(f_{c,90}/k_d \delta_d)^2 - (f_{c,90}/3k_d \delta_d) + (1/3)}{2 - (f_{c,90}/k_d \delta_d)} m_d.$$

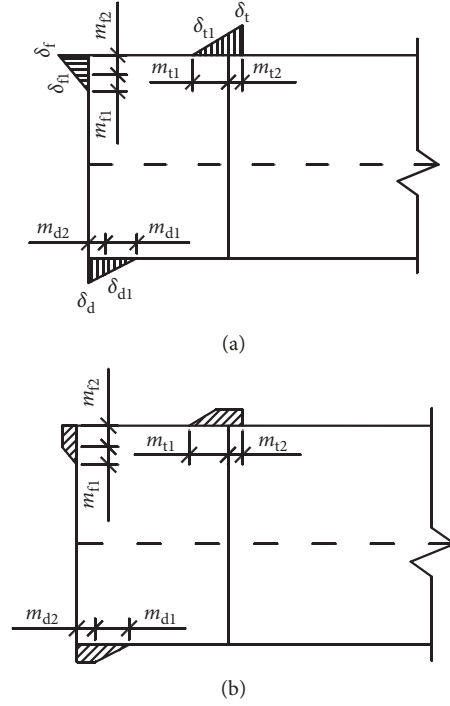


FIGURE 6: Deformation and stress distribution in local compression zones of the tenon. (a) Local compression deformation distribution and (b) local compression stress distribution.

The friction force corresponding to the compression area is as follows:

$$f_t = \mu N_t = \frac{b_s k_t}{2} \mu m_t \delta_t, \quad (13)$$

$$f_f = \mu N_f = \frac{b_s k_f}{2} \mu m_f \delta_f, \quad (13)$$

$$f_d = \mu N_d = \frac{b_s k_d}{2} \mu m_d \delta_d,$$

where $f_{c,90}$ is the compressive strength of the timber strip; b_s is the width of the tenon and when the tenon is damaged, the width of the tenon is defined as the original size minus any shrinkage; k_t , k_f , and k_d are the stress transformation coefficients of each zone; N_t , N_f , and N_d are the compression forces on the top, front, and bottom faces of the tenon, respectively; f_t , f_f , and f_d are the friction force on the top, front, and bottom compression areas of the tenon, respectively; y_{t1} , y_{d1} , and y_{f1} are the distances between the top, front, and bottom compression forces of the tenon head, respectively, and the center of the neck cross section under upward loading and unloading; and y_{t2} , y_{d2} , and y_{f2} are the distances between the top, front, and bottom compression forces of the tenon head, respectively, and the center of the neck cross section under downward loading and unloading. For downward loading and unloading, the t and d zones are simply exchanged in the formulas.

To calculate the resisting moment due to friction on the sides of the tenon, first, the deformation of the different sides must be determined, and then the corresponding stress

values can be obtained. From the stress values and geometric conditions, the friction moment between the sides of the tenon and the mortise can be obtained with reference to Figure 7.

The horizontal deformation at the middle of the tenon head can be obtained through its relationship with the amount of tenon slippage (Figure 7(a)):

$$\delta_e = \delta_0 \sin \alpha. \quad (14)$$

Further, stress on the sides of the tenon can be determined as follows:

$$\sigma_e = k_e \delta_0 = E_{c,90} \frac{\delta_0}{L_R} = \frac{E_{c,90}}{L_R} \delta_0, \quad (15)$$

where k_e is the extrusion compression conversion coefficient of the side of the tenon head, $E_{c,90}$ is the elastic modulus of the timber, and L_R is the length of the tenon head.

The cross-section compression deformation is assumed to be evenly distributed along the length of the tenon. Under upward loading and unloading (Figure 8(a)) and downward loading and unloading (Figure 8(b)), for the deformation region and the stress distribution on the sides of the tenon dovetail (Figure 8(c)), the larger the pullout force, the smaller the compression contact area, thus the compression stress is larger, but when the pullout force is smaller, the larger compression contact area is larger, thus the compression stress is smaller.

Taking the position "o" at the origin of the coordinates shown in Figure 8 as a reference, the compression deformation and stress in each section of the compression zone for upward deflection are given by equations (16) and (17), respectively, and for downward deflection are given by equations (18) and (19), respectively:

$$\delta_y = (\delta_0 - y \tan \theta) \sin \alpha, \quad (16)$$

$$\sigma_y = k_e \delta_y, \quad (17)$$

$$\delta_y = (\delta_0 + y \tan \theta) \sin \alpha, \quad (18)$$

$$\sigma_y = k_e \delta_y, \quad (19)$$

where δ_y is the extrusion deformation at the corresponding position along the height of the tenon; δ_0 is the amount of tenon pulling at the middle of the tenon neck; y the height on the tenon; θ is the rotation angle of the tenon; k_e is the compression stress conversion coefficient; and α is the tenon contraction angle.

The unit friction moment Δ_M in any microcell on the side of the tenon at coordinates x and y is as follows:

$$\Delta_M = \mu k_e (\delta_0 - y \tan \theta) \sin \alpha dx dy \sqrt{x^2 + y^2}. \quad (20)$$

The friction moment M_c can be obtained by integrating the bending moments for the upward loading bending moment as

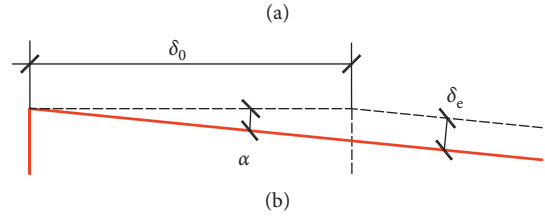
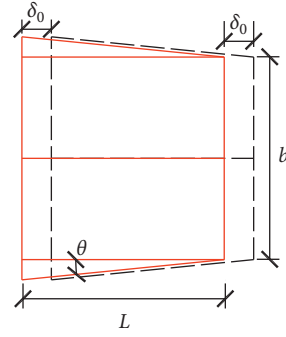


FIGURE 7: Side view of the tenon under (a) slippage and (b) contraction.

$$M = \int_{-(h_s/2)}^{h_s/2} \int_{(\delta_0 - y \tan \theta)/\cos \alpha}^{L/\cos \alpha} \mu k_e (\delta_0 - y \tan \theta) \cdot \sin \alpha \sqrt{x^2 + y^2} dx dy, \quad (21)$$

for the upward unloading bending moment as

$$M = - \int_{-(h_s/2)}^{h_s/2} \int_{\delta_0 - y \tan \theta / \cos \alpha}^{L/\cos \alpha} \mu k_e (\delta_0 - y \tan \theta) \cdot \sin \alpha \sqrt{x^2 + y^2} dx dy, \quad (22)$$

for the downward loading bending moment as

$$M = \int_{-(h_s/2)}^{h_s/2} \int_{\delta_0 + y \tan \theta / \cos \alpha}^{L/\cos \alpha} \mu k_e (\delta_0 + y \tan \theta) \cdot \sin \alpha \sqrt{x^2 + y^2} dx dy, \quad (23)$$

and for the downward unloading bending moment as

$$M = - \int_{-(h_s/2)}^{h_s/2} \int_{\delta_0 + y \tan \theta / \cos \alpha}^{L/\cos \alpha} \mu k_e (\delta_0 + y \tan \theta) \cdot \sin \alpha \sqrt{x^2 + y^2} dx dy. \quad (24)$$

Combining the geometric conditions, physical conditions, and balance and coordination conditions, the bending moment M of the joint can be obtained for the upward loading phase as

$$M = (f_t + f_d) \frac{h}{2} + f_f L + N_f y_{f1} + N_d y_{d1} - N_t y_{t1} + M_c, \quad (25)$$

for the upward unloading phase as

$$M = -(f_t + f_d) \frac{h}{2} - f_f L + N_f y_{f1} + N_d y_{d1} - N_t y_{t1} - M_c, \quad (26)$$

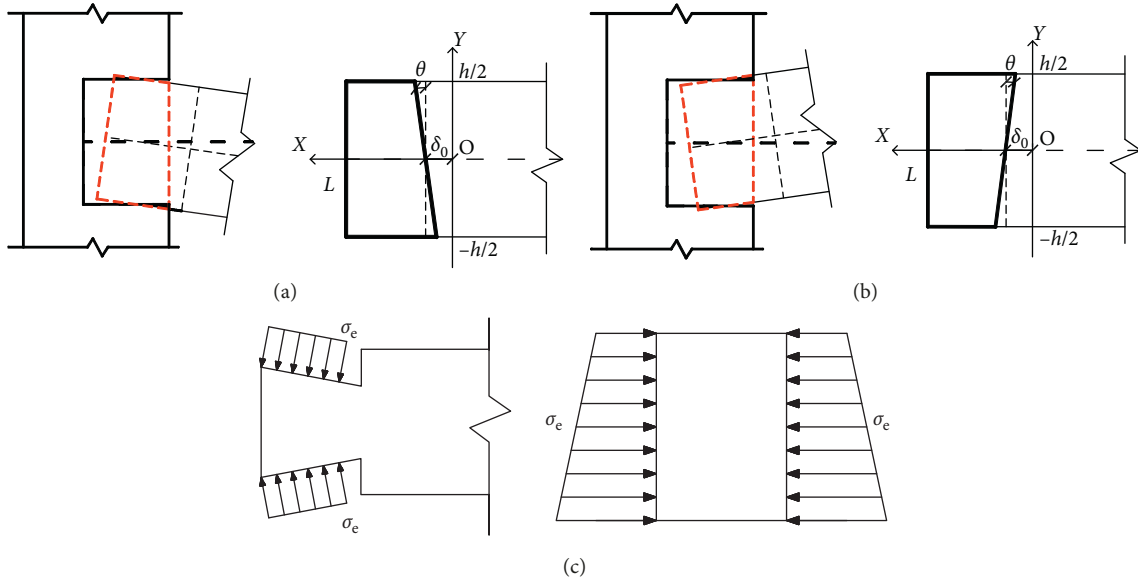


FIGURE 8: Tenon stress and deformation under extraction. (a) Upward loading (or unloading), (b) downward loading (or unloading), and (c) side extraction stress.

for the downward loading phase as

$$M = (f_t + f_d) \frac{h}{2} + f_t L + N_f y_{f2} + N_d y_{d2} - N_t y_{t2} + M_c, \quad (27)$$

and for the downward unloading phase as

$$M = -(f_t + f_d) \frac{h}{2} - f_t L + N_f y_{f1} + N_d y_{d1} - N_t y_{t1} - M_c, \quad (28)$$

where h is the height of the tenon and L is the length of the tenon.

3. Finite Element Simulation

3.1. Frame Design. The dimensions of the timber frame in the finite element simulation were determined according to [16]. To accommodate to the requirements of the “Creating Pattern” shape dialogue in ABAQUS, the frame was scaled to 1 : 3.52. The frame model dimensions are shown in Table 1.

Through investigation and research, three main reasons were identified for the slippage of mortise and tenon joints. First, a large horizontal load (such as that caused by large earthquakes or strong winds) applied at the joints can result in an excessive lateral displacement causing tenon pulling damage. Second, due to the influence of the natural environment, a change in the material properties of the tenon can cause contraction damage allowing the tenon to more readily rotate or slide out under the action of wind loads or small earthquakes. The third reason for slippage in mortise and tenon joints is the combination of the first two situations, referred to as mixed damage. The interaction between the mortise and tenon is different for different causes of tenon slippage. Therefore, in this study, each of the three cases, pulling, contraction, and mixing, damage was

evaluated individually. The slippage level was determined using the requirements for the assessment of “damage points” and the seismic structure requirements in the “*Technical Specifications for the Maintenance and Reinforcement of Ancient Timber Buildings.*” The slippage level was set at 1/5, 1/4, 3/10, 7/20, and 2/5 the length of the tenon head, as shown in Table 2.

In the finite element analysis, the column and tenon were modeled as solids and the bottom of the column was allowed to rotate only in the direction of loading to simulate the articulation of the column foot. The column was extended 150 mm higher than the strut to enable easy loading. The empty space in the joint was filled with a cork material in the referenced experiments. The interaction between the cork, the column, and the tenon is surface-surface contact: in the normal direction, it is hard contact, and in the tangential direction, it is Coulomb friction with a coefficient is 0.3. In order to optimize both the computational efficiency and accuracy, an eight-node linear hexahedron element (C3D8R) was used to model the solids. In the mortise and tenon joint areas, the mesh was refined to improve the accuracy in this area of interest. The complete finite element model is shown in Figure 9.

3.2. Definition of Wood Properties. In this study, the timber was considered to be northeast Korean pine and finite element code ABAQUS was utilized to obtain numerical simulations of wooden frame with dovetail mortise and tenon joints. Timber is a typical orthotropic anisotropy material with the simplified constitutive model (Figure 10), where ϵ_{cy} is the yield strain under compression, ϵ_{cu} is the ultimate compressive strain, ϵ_{tu} is the ultimate tensile strain, f_{cy} is the compressive strength, and f_{tu} is the tensile strength.

Wood can be divided in radial, chordwise, and longitudinal directions, each with different physical and

TABLE 1: Frame dimensions.

Column			Strut	
Diameter (mm)	Height (mm)	Length (mm)	Width (mm)	Height (mm)
210	1650	1400	120	180

TABLE 2: Simulation parameters for different tenon sizes and pulling levels.

Damage type	Specimen number	Slippage proportion	Applied tenon pulling damage (mm)	Applied tenon contraction damage (total, two sides) (mm)	Width of tenon head after pullout (mm)	Width of tenon neck after pullout (mm)	Length of tenon (mm)
Intact	W1	0	0.00	0.00	60.0	50.0	50
	Q1	1/5	10.00	1.00	58.0	48.0	50
	Q2	1/4	12.50	1.25	57.5	47.5	50
Contraction	Q3	3/10	15.00	1.50	57.0	47.0	50
	Q4	7/20	17.50	1.75	56.5	46.5	50
	Q5	2/5	20.00	2.00	56.0	46.0	50
	L1	1/5	10.00	0.00	*	50.0	50
	L2	1/4	12.50	0.00	*	50.0	50
Pulling	L3	3/10	15.00	0.00	*	50.0	50
	L4	7/20	17.50	0.00	*	50.0	50
	L5	2/5	20.00	0.00	*	50.0	50
	LQ1	1/5	10.00	0.50	*	49.0	50
	LQ2	2/5	20.00	1.00	*	48.0	50
Mixed	LQ3	3/10	15.00	0.50	*	49.0	50
	LQ4	3/10	15.00	1.00	*	48.0	50

Note. The proportions of pulling : contraction damage in LQ1–LQ4 are 1 : 1, 1 : 1, 2 : 1, and 1 : 2, respectively.

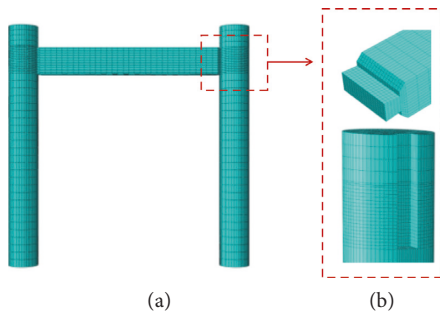


FIGURE 9: Meshes of (a) column frame and (b) mortise and tenon joint.

mechanical characteristics. The material behavior in the elastic phase in ABAQUS was defined by the nine engineering constants shown in Table 3 [16], in which the E values represent the elastic constants in the three orthogonal directions, the ν values represent Poisson's ratios in their respective directions, and the G values represent the shear moduli in their respective directions. In this model, the directions 1, 2, and 3 represent the radial, chordwise, and longitudinal axes, respectively, of the strut framing into the column.

After entering the plastic stage, Hill's potential function in the property module can be used to define the yield criterion of the timber. By defining the yield stress ratios in six directions to consider the difference in the yield strength of the material in three orthogonal directions, [16] can be used to obtain the yield stress ratios shown in Table 4.

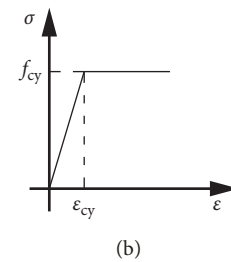
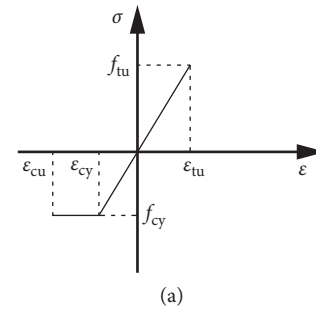


FIGURE 10: Simplified constitutive model of timber. (a) Parallel to the grain; (b) compression in radial direction.

3.3. Loading System. To simulate the presence of a roof, a vertical load of 10 kN was applied to the top of each column and a horizontal cyclic load was applied at the top of one of the columns using displacement control. After the good results in [16], the maximum loading displacement was set to about 0.2 m after scaling. The applied displacement amplitude of this test is shown in Figure 11.

TABLE 3: Northeast red pine wood constants.

E_1 (MPa)	E_2 (MPa)	E_3 (MPa)	u_{12} (-)	u_{13} (-)	u_{23} (-)	G_{12} (MPa)	G_{13} (MPa)	G_{23} (MPa)
650	275	10000	0.035	0.02	0.02	210	650	275

TABLE 4: Yield stress ratios.

R11	R22	R33	R12	R13	R23
0.2	0.2	1	1	0.35	0.2

Note. Dimensionless.

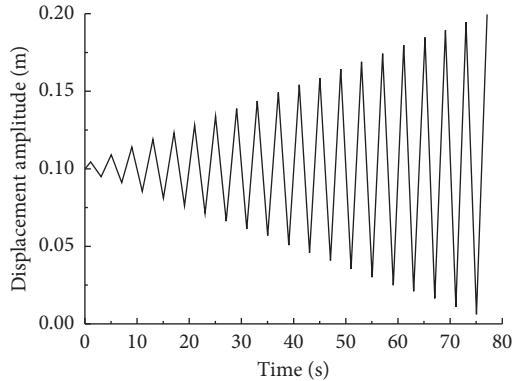


FIGURE 11: Horizontal displacement loading amplitude.

The frame was first loaded by the vertical load and then by the horizontal load as follows. For the pullout damage and mixed damage frame tests, the column was drawn to the one side until it reached the specified deflection. For the contraction damage test, the degree of contraction, defined as when the tenon and the mortise contacted each other without gaps, was used to determine the applied deflection. The same loading modes were applied to the intact joint.

3.4. Comparison of Simulation Results with Test Results and Theoretical Calculation. The finite element simulation was designed based on a real experiment, so the simulation of the column frame can be verified by the results in [16]. The bending moment-angle hysteresis curves given in the reference are shown in Figures 12(a)–12(c). The hysteresis curve of the frame obtained from the finite element simulation is shown in Figure 12(d), and a comparison of the results of the theoretical calculations and the finite element simulation is shown in Figure 13.

It can be seen that the simulation results are in good agreement with the experimental results in which loading deflection was 100 mm. Furthermore, the comparison between the theoretical calculation and the numerical simulation shown in Figure 13(a) also indicates good agreement. Taking into account the discreteness of wood properties and the potential for test errors, the theoretical calculations and numerical simulations are clearly sufficiently effective in replicating the experimental results.

The results of the proposed theoretical calculation method considering the change in the loading and in the size of the tenon head for frames with 1/5 pullout damaged joints and a similar degree of cutting damaged joints are compared with the simulation results at the 100 mm loading stage in Figures 13(b)–13(d). The reduction of the friction moment caused by contraction damage is significantly greater than that caused by a similar degree of pullout damage. When the degree of pullout damage is the same, contraction damage still controls the behavior, which is consistent with the conclusions of the previous analysis.

4. Simulation Results Extension Analysis

4.1. M - θ Hysteresis Curve. The hysteresis curve provided by the parametric analysis depicts the relationship between the resisting moment and the rotation angle of the joints. In Figure 14, L1–L5 show the bending moment-angle hysteresis curves of the joints under different degrees of pulling damage; Q1–Q5 are for different degrees of contraction damage and LQ1–LQ4 are for different proportions of mixed pulling and contraction damage. These hysteresis curves are compared to the hysteresis curve of the intact joint W1.

It can be observed that the behavior of Frames L1–L4 is similar to that of W1 in general, with a maximum bending capacity of around 1.6 kN·m. The hysteresis curves of the frames with pulling damage have a spindle shape in the initial stage of loading. The larger the deflection, the greater the fullness of the curve. In the later stages, the overall stiffness of the frame is relatively large, and the energy dissipation effect is good. The main reason for this is that in the process of forming a pulling failure, the tenon is compressed against the mortise, increasing the initial compression force between the tenon and the mortise along with the friction force at the contact surface, enhancing the rigidity of the joint. The drop in the peaks of several subsequent cycles was due to the sliding of the tenon. The hysteresis curves under continued loading show that when the lateral displacement is sufficiently large, the difference in deflection has little effect on the seismic performance of the frame. The hysteresis curves of Frames Q1–Q4 with contraction damage are flat and the bearing capacities are significantly lower than those of W1. The larger the extent of contraction damage, the more the substantial this reduction is. After the column frame is stressed, the tenon rotation relative to the column is close to 0.06 rad, the bending stiffness slightly increases, and the maximum bending capacity is about 0.75 kN·m. The reason for this change is that the size of the tenon is decreased as a result of contraction damage, meaning that the tenon surfaces make almost no contact with the

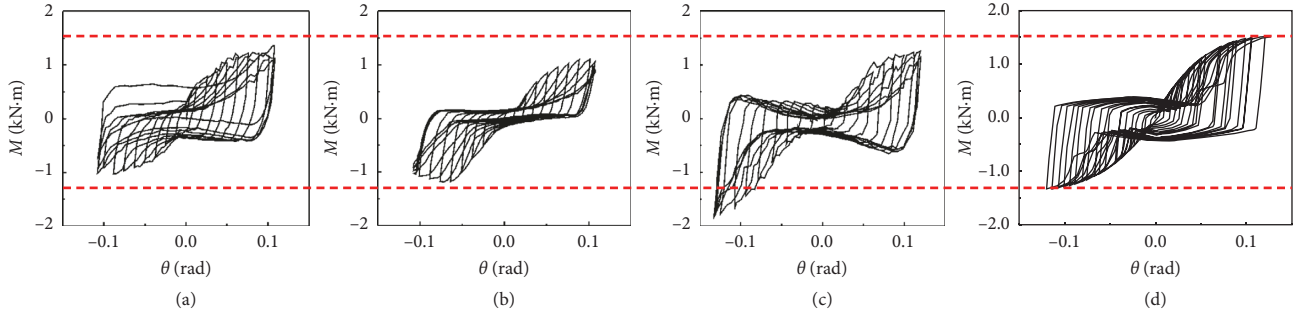


FIGURE 12: Hysteresis curves of (a)–(c) reference tests and (d) simulation.

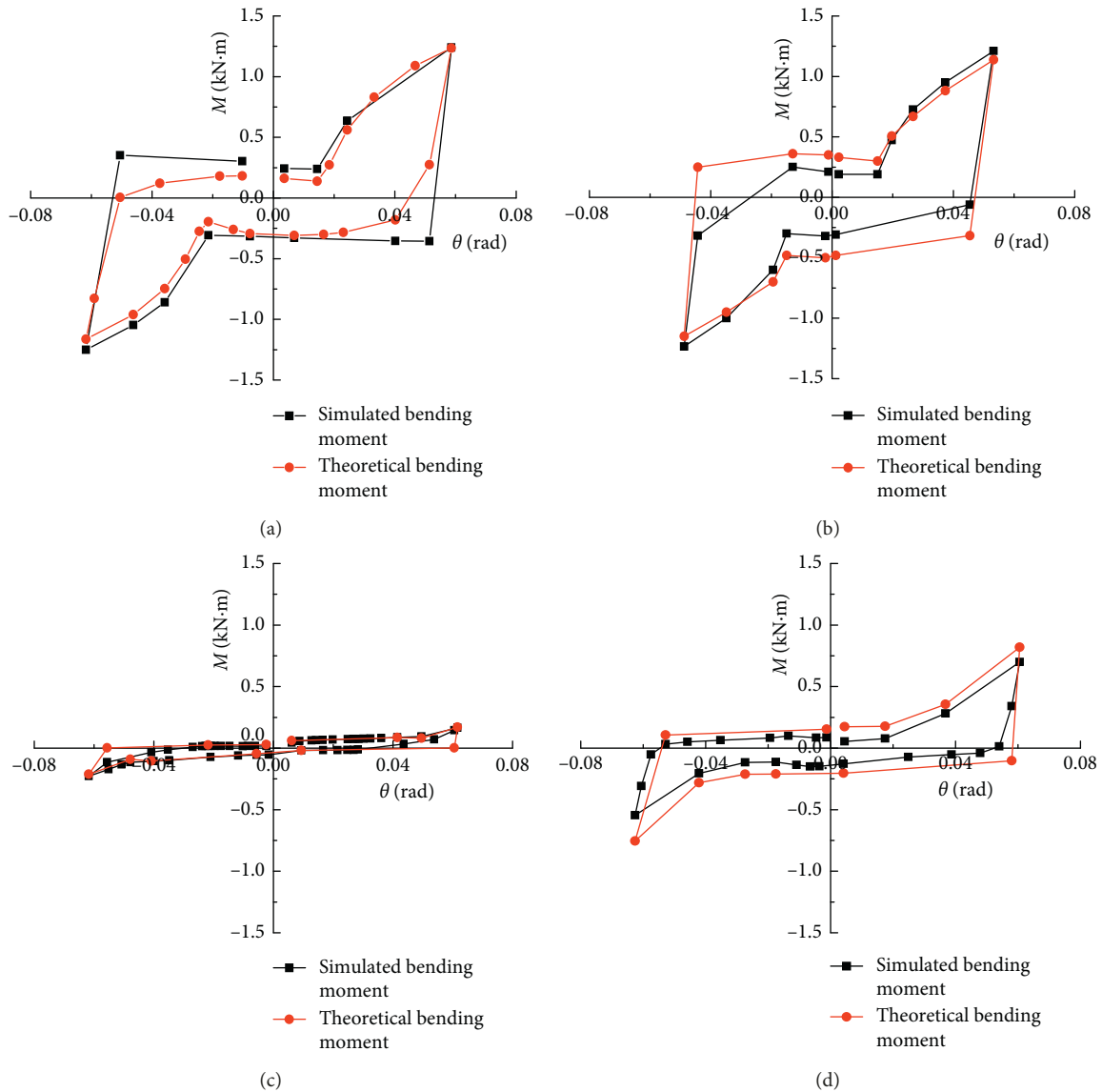


FIGURE 13: Comparison of bending moments from the proposed theoretical calculation and the simulation. (a) No damaged joint, (b) pulling damaged joint, (c) contraction damaged joint, and (d) mixed damage joint.

surfaces of the mortise, so there is only a small friction force between the upper and lower surfaces and the bottom of the mortise. When the axial force in the strut is

greater than the friction between the mortise-tenon, the tenon will slide, and when the rotation angle reaches at 0.06 rad, the tenon slides into the deeper part of the

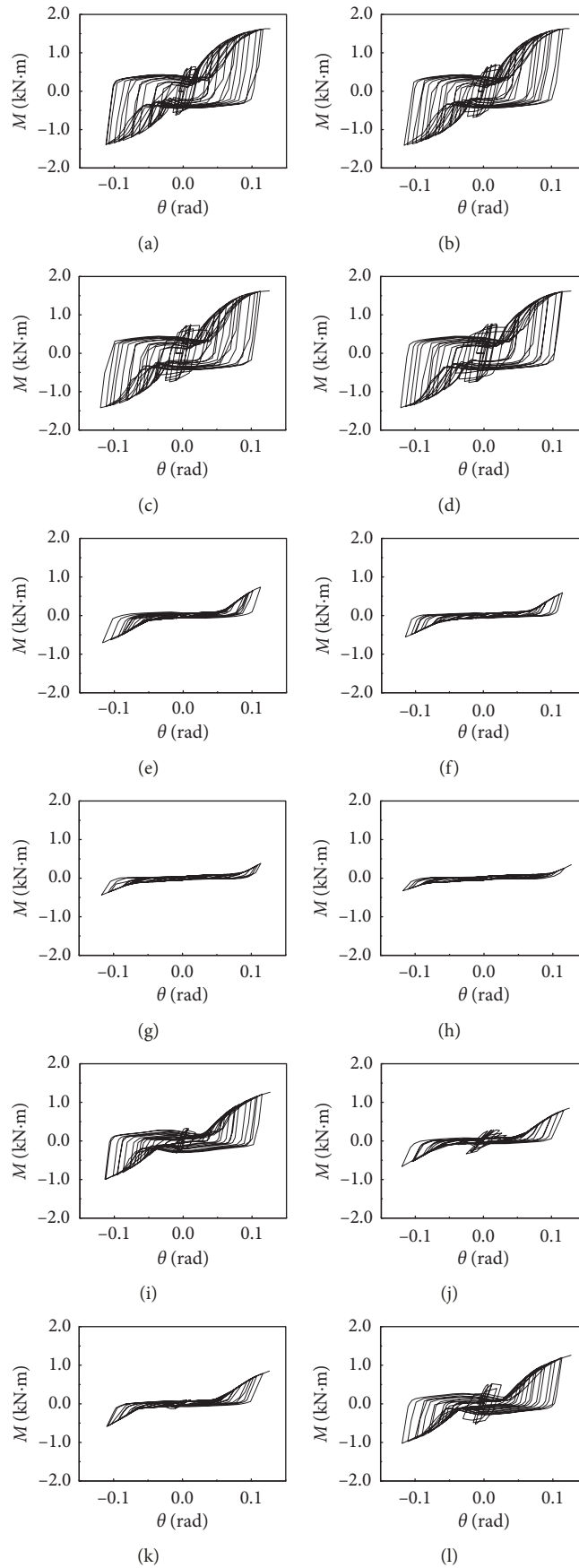


FIGURE 14: The $(M-\theta)$ hysteresis curves for all damage models. (a) L1, (b) L2, (c) L3, (d) L4, (e) Q1, (f) Q2, (g) Q3, (h) Q4, (i) LQ1, (j) LQ2, (k) LQ3, and (l) LQ4.

mortise where the inside of the mortise and the front face of the tenon finally come into contact. During the rotation of the joint, the frictional force generated by this contact increases the resistance moment of the joint.

The hysteresis curve of the mixed damage frame combines the characteristics of frames with pulling and contraction damage. The deflection of Frame LQ1 is the same as that of Frames L1 and Q1. The stiffness at the initial stage of loading is large, and then sliding of the tenon occurs, causing the bearing capacity to decrease. At this stage, the shape of both Frames LO1 and L1 changes similarly, but the stiffness of LO1 is significantly smaller and is affected by the contraction-reduced size of the tenon, as the performance of a joint depends on the compression forces within the joint and the associated friction to limit its rotation and sliding. The entire hysteresis of the LO1 curve is located within those of L1 and Q1. The behavior of Frame LQ2 is consistent with that of Frames L5 and Q5 at similar deflections. In this case, although in the proportion of pulling to contraction damage, the pulling damage is equal, the load capacity of the mixed damage joint is clearly smaller. The development of the hysteresis curve of Frame LO2 is also within that of L5 and Q5 but closer to Q5. The joint in Frames LQ3 and LQ4 both have the same degree of pulling damage of 3/10, similar to Frames L3 and Q3, and their hysteresis curves are accordingly between those of L3 and Q3. The comparison of the performance of Frames LQ1 and LQ3 and Frames LQ2 and LQ4 indicates that although the total applied deflection is different, the hysteresis characteristics are similar when the combined contribution of pulling and contraction damage is the same.

4.2. M - θ Skeleton Curve. Figure 15 depicts the frame bending moment-rotation (M - θ) skeleton curves for each joint damage type.

The bending moment in the joint can be observed to increase with the increase in the rotation angle during the loading of the frame W1 and does not decrease until the loading is complete, exhibiting excellent capacity. From the change in the slope of the skeleton curve, it can be inferred that the joint exhibits different stiffnesses during rotation: when the rotation angle is small, the squeezing between the mortise and tenon is tight and the bending stiffness is large, but as the rotation angle increases, the sliding of the tenon increases as well, some plastic deformation occurs, and the stiffness of the joint decreases. The stability of the load capacity in the later stages indicates that an undamaged mortise and tenon joint generally provide good ductility.

The skeleton curves of frames L1–L5 with pulling damaged joints are initially “S” shaped. The linear change from the start of loading to the first turning point is due to the fact that the increasing internal compression forces cause the friction force to increase, delaying the sliding of the tenon head, keeping the joint in the elastic deformation stage. The “S” shaped top descending segment is caused by the sliding of the tenon when the friction force between the mortise and tenon is smaller than the axial force in the

strut. After this segment, the behavior of these frames is close to that of the intact column frame, and the difference in the degree of tenon pullout is very small. Compared to the frames with intact and pulling damaged joints, the capacities of the frames with contraction damaged joints were significantly smaller. The bending moments of Frames Q1 and Q2 at the joints increase after a rotation of 0.06, exhibiting a maximum bending moment only 40% that of the intact column frame. The variation in capacity of frames Q3–Q5 is very small, though generally the capacity of the frame gradually decreases with the increase in applied deflection.

In Figure 15(c), it can be seen that the skeleton curves of the frames with mixed damage joints are between those of the frames with pulling damaged and cutting damaged joints under the same deflection. The skeleton curves of LQ1 and LQ3, and LQ2 and LQ4 for different deflections basically coincide after a rotation of 0.04, and the resistance moment of Frame LQ3 is greater than that of LQ2, i.e., the capacity does not exhibit any correlation to the deflection. The effects of the same deflection on frames with the same degree of contraction damage in the Q and LQ groups were the same, indicating that cutting damage plays a significant role in determining the effects of joint damage on the frame behavior.

4.3. Energy Dissipation. The relationship between the equivalent viscous damping coefficient and the rotation angle of the frames with intact and pulling damaged joints is shown in Figure 16, indicating an equivalent viscous damping coefficient of 0.25 at 0.06 rad. The energy consumption of the frame with pulling damaged joints is greater than that of the frame with the intact joints, but the energy dissipation capacity decreases as the rotation angle increases, and the equivalent viscous damping coefficient value finally stabilizes at around 0.25. The viscous damping coefficients of frames with pulling damaged joints are clustered around at 0.02–0.045 rad, and the energy dissipation capacity is maintained at a relatively high level or even increases. This indicates that the increase in the compression force between the mortise and tenon can increase the energy consumption of the joint.

Note that the area within the hysteresis curve of all frames with contraction damaged joints is much smaller than within those of frames with intact and pulling damaged joints. When the degree of joint pulling allowed by the contraction of the tenon material exceeds 1/5, the joints basically lose their energy dissipation ability. Frames LQ1 and LQ3, which have a small amount of pulling damage relative to contraction damage, exhibit an energy dissipation capacity between the pulling and contraction damaged joints. Frames LQ2 and LQ4 are also similar. This is due to the fact that cutting damage to the tenon weakens the contact friction between the mortise and tenon, reducing the friction energy consumption, which is an important component of the energy consumption of the joint.

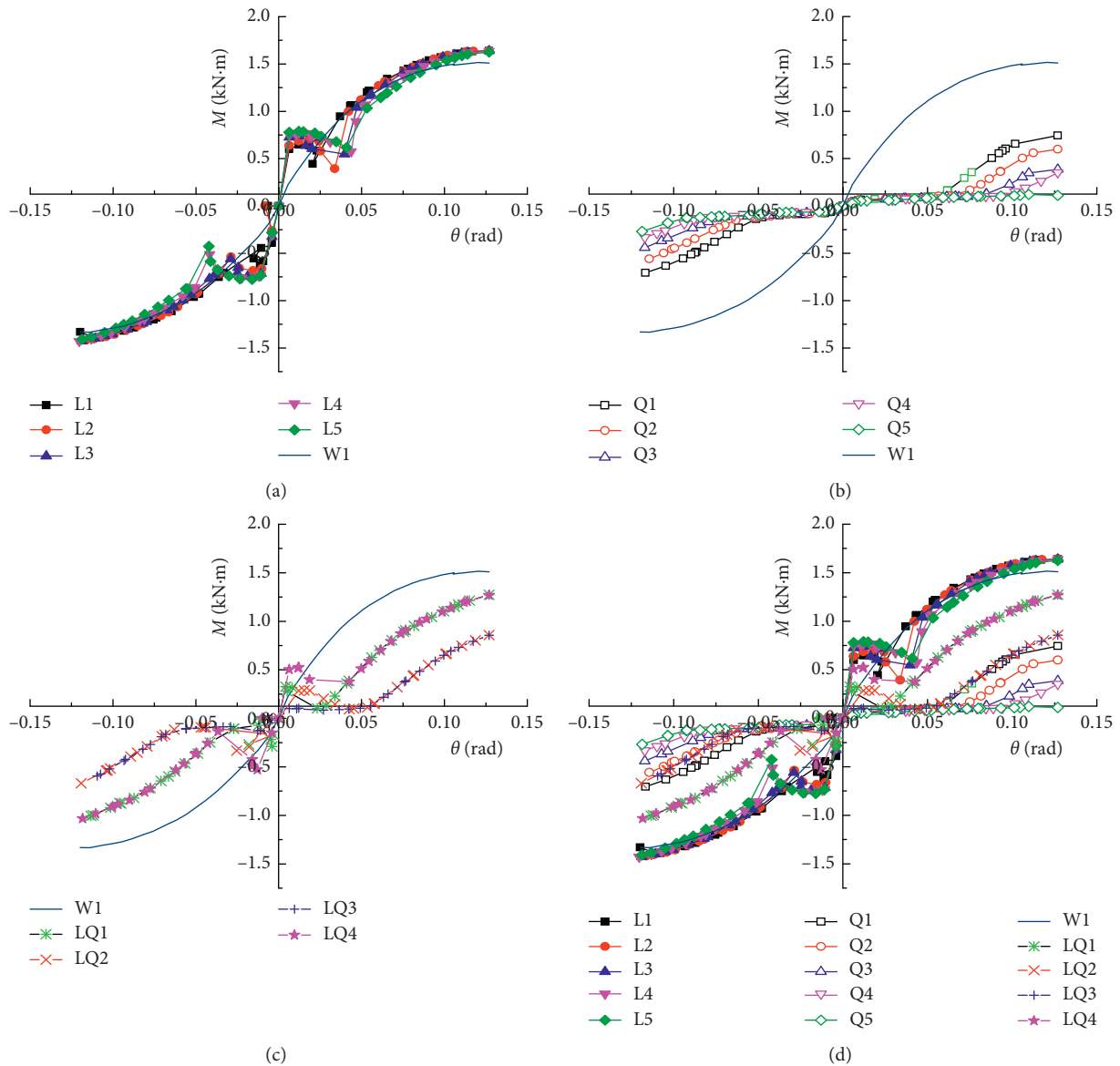


FIGURE 15: Bending moment-angle (M - θ) skeleton curves. (a) Pulling damaged and intact frame skeleton curves, (b) contraction damaged and intact frame skeleton curves, (c) mixed damaged and intact frame skeleton curves, and (d) all frame skeleton curves.

4.4. Relationship between Bending Moment and Deflection.

The relationships between the bending moments in the joints and deflections applied to the frames are shown in Figure 17. When the frames with pulling damage are deflected such that the joints rotate about 0.04 rad, the bending moment of the joints decreases significantly as the applied deflection increases, but deflection has no significant influence on the bending moment of the joint at other angles. The deflection applied to the contraction damaged frames at joint angles less than 0.06 rad has little effect on the bending moment, but above 0.06 rad, the bending moment decreases significantly with increasing deflection. When the proportion of pulling to contraction damage is close to one in frames with mixed damage joints, the bending moment gradually decreases with increasing applied deflection at each stage of

frame behavior; when the proportion of contraction damage is smaller and the joints are rotated at different angles, the bending moment values are consistently larger.

4.5. Deform Ability. There was no significant yield point after the frames were sufficiently stressed. The increase in bending moment gradually decreased after the frames with intact and pulling damaged joints were deformed about 0.05 rad until reaching 0.12 rad, during which time the capacity did not decrease and the column frame ductility was better. As the bending moments applied to frames with contraction damaged and mixed damaged joints began to increase, the deformation of the frames was comparatively larger than that of the frames with intact and pulling damaged joints. From the overall view of the frame, a joint

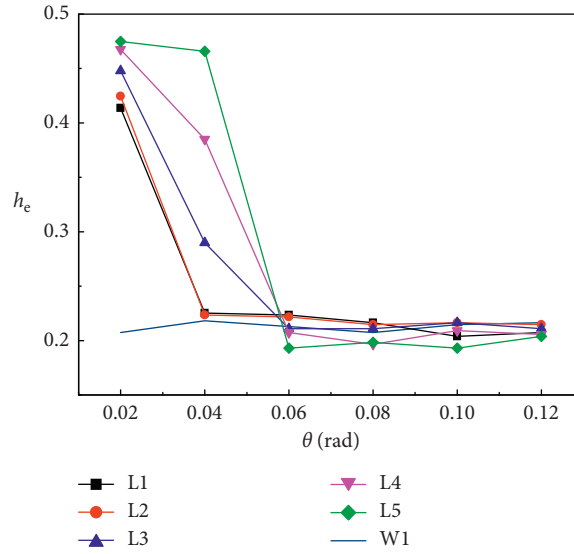


FIGURE 16: Equivalent viscous damping coefficient of frames with pulling damaged joints.

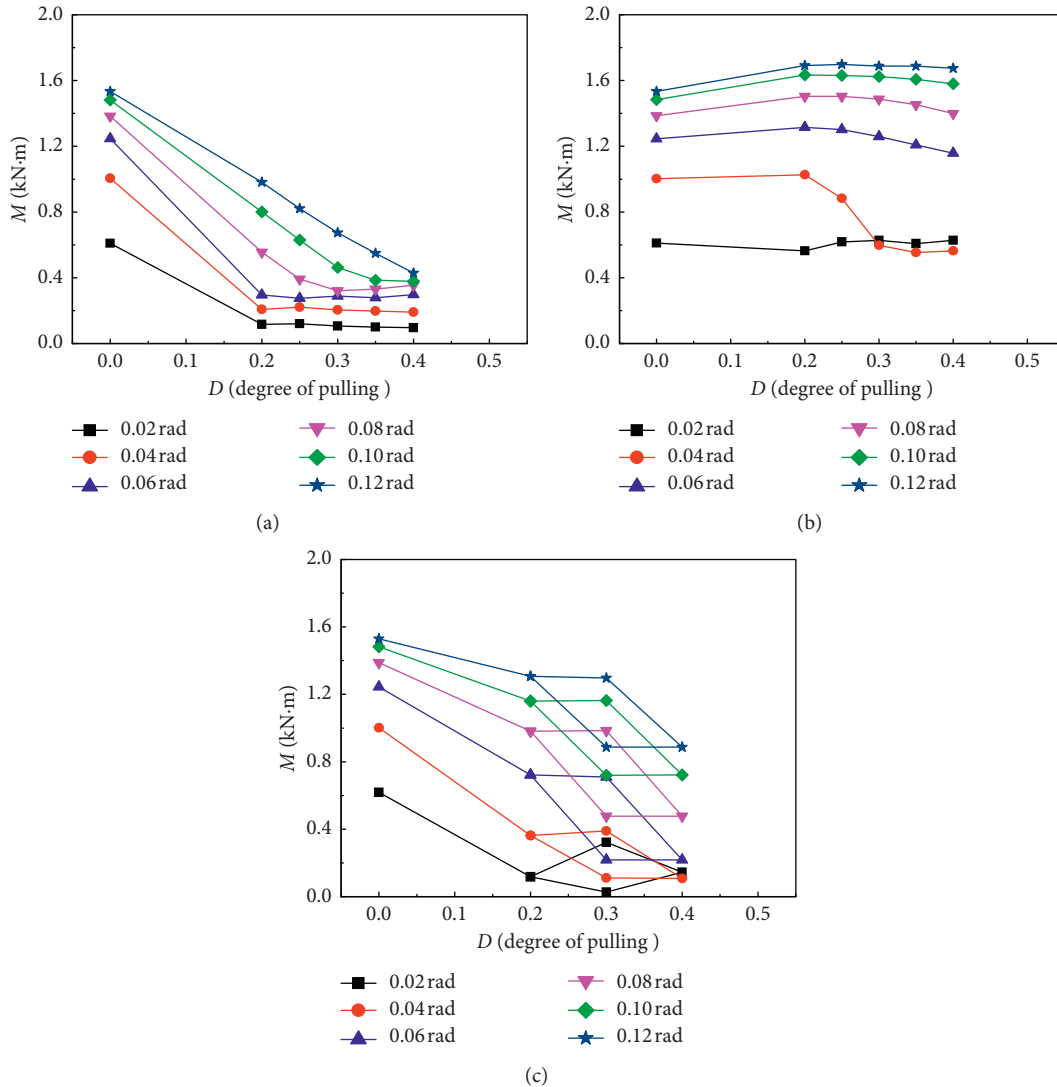


FIGURE 17: Relationship between bending moment and degree of slippage of the (a) pulling damaged frame, (b) contraction damaged frame, and (c) mixed damage frame.

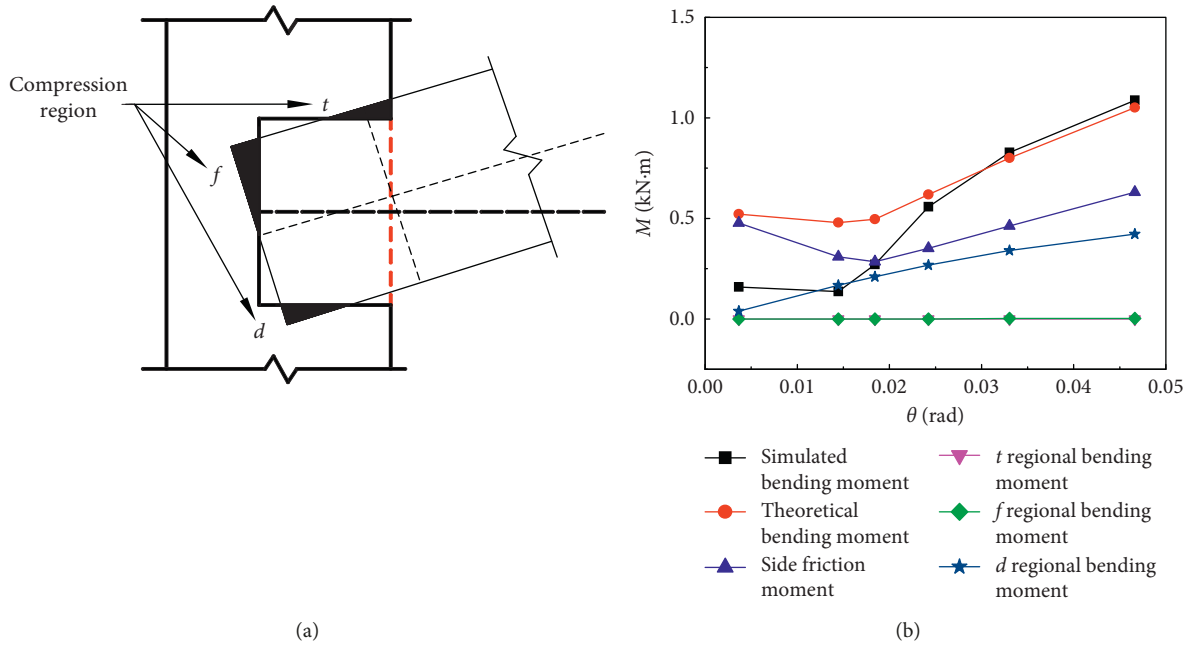


FIGURE 18: Bending moment distribution between joint areas. (a) Rotated joint and (b) moment contribution of each area.

rotation angle of 0.12 rad (0.2 m) at the end of loading was greater than 1/30 (0.033 rad), the limiting rotation angle of a timber member provided in the specification, which is also greater than the overall “damage point” of timber components when evaluated with a limit of 0.016 m for a building structure with a seismic tilt limit of 0.014 m and 0.035 m (for a fortification intensity of 8 and 9 degrees, respectively).

4.6. Sources of Bending Moment Resistance. Combining the relevant geometry and physical parameters of the frame, the loading amplitude was set to 100 mm per cycle. For the intact column frame, the upward loading mode is taken as an example. The different contact sites and bending moment contribution trends with respect to rotation angle are shown in Figures 18(a) and 18(b).

In the upward loading stage, the moment due to contact and the moment due to friction at the contact point rapidly increase, causing the bending moment to increase rapidly with the increase in the rotation angle. As the rotation angle continues to increase, the tenon begins to slip in the mortise, and the amount of tenon pulling is increased. With this increase, the moment continues to increase but at a significantly reduced rate. The bending moment then drops rapidly when upward unloaded, and the compression and friction forces change little as the frame continues to unload. The main direction of load change is in the direction of the friction force, indicating that the lateral friction bending moment accounts for the bending moment in the entire joint. The additional bending moment created by the vertical load applied to the top of the column must be balanced by horizontal tension during the unloading of the column. During the unloading process, the deformation of the compression zone gradually decreases and slip occurs between the mortise and tenon.

TABLE 5: Percentage of bending moment contribution from each area.

Angle (θ)	T (%)	d (%)	f (%)	Side friction (%)
0.0036	4.53E-05	8.00	0	91.99
0.0144	0.00311	35.10	0	64.89
0.0184	0.00627	42.88	0	57.10
0.0243	0.01161	43.41	0.10	56.46
0.0332	0.02297	42.38	0.40	57.19
0.0467	0.04900	39.96	0.20	59.79

Table 5 details the changes in the distribution of bending moments between various parts of the joint. The proportion of side friction moments in the joint exceeds half of the total bending moment value at all times, especially when the contact area between the tenon head and the mortise wall is larger. When damage occurs in these areas, the joint will less effectively resist the bending moment.

5. Conclusions

- (1) Through an analysis of the forces in a timber mortise-tenon joint, a theoretical equation for calculating the resisting moment of the joint was established that can account for joint damage.
- (2) The theoretical calculations and numerical simulations indicate that when the degree of pulling damage to a joint is within 2/5 of the length of the joint, the same applied deflection results in only a small difference in frame behavior compared to that of a frame with intact joints, while a similar degree of contraction damage causes the stiffness of the frame and joint to decrease significantly compared to that of a frame with intact joints, and the load-carrying capacity and resistance of a frame with mixed damage joints are

between those of a frame with intact joints and a frame with contraction damaged joints.

- (3) The evaluated dovetail mortise and tenon joints exhibit a good semirigid character. The seismic performance of a frame with pulling damaged joints is not significantly different from that of a frame with intact joints; the seismic performance of a frame with contraction damaged joints is significantly weakened, with the joint losing half of its rigidity, while the seismic performance of a frame with mixed damaged joints is controlled by the proportion of pullout damage to contraction damage. The higher the proportion of contraction damage, the weaker the seismic performance.
- (4) The friction force between the tenon and mortise is the main source of bending moment resistance and energy consumption. The moment generated by the lateral friction contributes more than 50% of the overall bending moment resistance of the joint.
- (5) This paper sets the wood properties and the finite element model according to the ideal state. Some simplified calculation methods are used in the calculation of bending moments, and the accuracy of the results can still be optimized.
- (6) This paper carried out numerical simulations without experiments and only studied a single dovetail joint. Using this theory in the overall structural simulation analysis will provide greater help in assessing structural damage.

Notations

t, d, f :	Contact areas of the top, bottom, and front surfaces of the tenon head
N_t, N_f, N_d :	Compression forces on the top, front, and bottom faces of the tenon
f_t, f_f, f_d :	Friction force on the top, front, and bottom compression areas of the tenon
$\delta_t, \delta_f, \delta_d$:	Maximum deformation in each compression zone
$\delta_{t1}, \delta_{f1}, \delta_{d1}$:	Deformation corresponding to the ultimate compressive strengths of the crushed zones
m_{t1}, m_{d1}, m_{f1} :	Length of the elastic zones in t, d , and f
m_{t2}, m_{d2}, m_{f2} :	Elastic and plastic zones in t, d , and f
y_{t1}, y_{d1}, y_{f1} :	Distances between the top, front, and bottom compression forces of the tenon head and the center of the neck cross section under upward loading and unloading
y_{t2}, y_{d2}, y_{f2} :	Distances between the top, front, and bottom compression forces of the tenon head and the center of the neck cross section under downward loading and unloading
k_t, k_f, k_d :	Stress transformation coefficients of each zone
L_s, h_s, b_s :	Length, height, width of the tenon
θ :	Rotation angle of the joint

δ_0 :	Extracted displacement of the tenon from the mortise
Δ_u, Δ_l :	Extracted displacements at the upper and lower faces of the tenon
Δ_e :	Initial displacement
K_e :	Extrusion compression conversion coefficient
Δy :	Extrusion deformation at the corresponding position along the height of the tenon
Σe :	Stress on the sides of the tenon
Σy :	Compression stress of the compression zone
$f_{c,90}$:	Compressive strength of the timber strip
$E_{c,90}$:	Elastic modulus of the timber
L_R :	Length of the tenon head
ΔM :	Unit friction moment
M_C :	Friction moment
E_{cy} :	Yield strain under compression
E_{cu} :	Ultimate compressive strain
E_{tu} :	Ultimate tensile strain
F_{cy} :	Compressive strength
F_{tu} :	Tensile strength.

Data Availability

The program data used to support the findings of this study are available from the corresponding author upon request.

Conflicts of Interest

The authors declare that they have no conflicts of interest.

Acknowledgments

The authors would like to acknowledge the financial support from the National Key Research and Development Program of China (project no. 2016YFC0701500).

References

- [1] C. Bedon, M. Fragiocomo, C. Amadio, M. ASCE, and C. Sadoch, "Experimental study and numerical investigation of blockhaus shear walls subjected to in-plane seismic loads," *Journal of Structural Engineering*, vol. 141, no. 4, article 04014118, 2015.
- [2] J. M. Branco and J. P. Araújo, "Structural behaviour of log timber walls under lateral in-plane loads," *Engineering Structures*, vol. 40, pp. 371–382, 2012.
- [3] D. F. D'Ayala and P. H. Tsai, "Seismic vulnerability of historic Dieh-Dou timber structures in Taiwan," *Engineering Structures*, vol. 30, no. 8, pp. 2101–2113, 2008.
- [4] R. J. Leichti, R. A. Hyde, M. L. French et al., "The continuum of connection rigidity in timber structures," *Wood and Fiber Science*, vol. 32, no. 1, pp. 11–19, 2000.
- [5] Y. H. Chui and Y. Li, "Modeling timber moment connection under reversed cyclic loading," *Journal of Structural Engineering*, vol. 131, no. 11, pp. 1757–1763, 2005.
- [6] C. L. O. Santana and N. T. Mascia, "Wooden framed structures with semi-rigid connections: quantitative approach focused on design needs," *Structural Engineering and Mechanics*, vol. 31, no. 3, pp. 315–331, 2009.

- [7] D. P. Fang, S. Iwasaki, M. H. Yu, Q. P. Shen, Y. Miyamoto, and H. Hikosaka, "Ancient Chinese timber architecture. I: experimental study," *Journal of Structural Engineering*, vol. 127, no. 11, pp. 1348–1357, 2001.
- [8] W. S. King, J. Y. R. Yen, and Y. N. A. Yen, "Joint characteristics of traditional Chinese wooden frames," *Engineering Structures*, vol. 18, no. 8, pp. 635–644, 1996.
- [9] J. Y. Xue, Z. J. Wu, F. L. Zhang, and H. T. Zhao, "Seismic damage evaluation model of Chinese ancient timber buildings," *Advances in Structural Engineering*, vol. 18, no. 10, pp. 1671–1683, 2015.
- [10] H. Huang, Z. Sun, T. Guo, and P. Li, "Experimental study on the seismic performance of traditional Chuan-Dou style wood frames in Southern China," *Structural Engineering International*, vol. 27, no. 2, pp. 246–254, 2017.
- [11] Z. Yue, "Traditional Chinese wood structure joints with an experiment considering regional differences," *International Journal of Architectural Heritage*, vol. 8, no. 2, pp. 224–246, 2014.
- [12] X. Li, J. Zhao, G. Ma, and S. Huang, "Experimental study on the traditional timber mortise-tenon joints," *Advances in Structural Engineering*, vol. 18, no. 12, pp. 2089–2102, 2015.
- [13] X. Li, J. Zhao, G. Ma, and W. Chen, "Experimental study on the seismic performance of a double-span traditional timber frame," *Engineering Structures*, vol. 98, pp. 141–150, 2015.
- [14] J. H. Zhao, M. H. Yu, D. F. Gao, and J. B. Sun, "FEM analysis on the elasto-plasticity of ancient wooden structure," *Journal of Xi'an University of Architecture & Technology (Natural Science Edition)*, vol. 31, no. 2, pp. 131–133, 1999, in Chinese.
- [15] Y. P. Dong, R. X. Zhai, M. H. Yu, and R. L. Yu, "Reasons for northward descent of baoguo temple hall in Ningbo," *Sciences of Conservation and Archaeology*, vol. 15, no. 4, pp. 1–5, 2003, in Chinese.
- [16] H. B. Wu, "Finite element analysis of stiffness of dovetail nodes in ancient buildings," *Sichuan Building Materials*, vol. 41, pp. 42–43, 2015, in Chinese.
- [17] T. Y. Zhou, W. M. Yan, X. Y. Zhou, and B. Zhang, "Analysis on velocity vibration characteristics of stator of radial piston pump," *Advanced Materials Research*, vol. 230–232, no. 6, pp. 679–684, 2011, in Chinese.
- [18] Q. F. Xie, B. Du, F. L. Zhang, P. J. Zheng, and Q. F. Xu, "Study on the moment-rotation model of the dovetail mortise-tenon joint of ancient timber building," *Engineering Mechanics*, vol. 31, no. 12, pp. 140–146, 2014.
- [19] J.-M. Seo, I.-K. Choi, and J.-R. Lee, "Static and cyclic behavior of wooden frames with tenon joints under lateral load," *Journal of Structural Engineering*, vol. 125, no. 3, pp. 344–349, 1999.
- [20] Y. Kato and K. Komatsu, "Strength and deformation of semi-rigid timber frames depending on the embedment resistance of timber," *Wood Research*, vol. 87, pp. 39–41, 2000.
- [21] Z. W. Guan, A. Kitamori, and K. Komatsu, "Experimental study and finite element modelling of Japanese "Nuki" joints—part one: initial stress states subjected to different wedge configurations," *Engineering Structures*, vol. 30, no. 7, pp. 2032–2040, 2008.
- [22] S.-J. Pang, J.-K. Oh, J.-S. Park, C.-Y. Park, and J.-J. Lee, "Moment-carrying capacity of dovetailed mortise and tenon joints with or without beam shoulder," *Journal of Structural Engineering*, vol. 137, no. 7, pp. 785–789, 2011.
- [23] Y. Wu, X. D. Guo, X. S. Song, and X. Yong, "Experimental study on mechanical behavior of dovetail joint in historic buildings out of mortise," *Journal of Guangxi University: Natural Science Edition*, vol. 39, no. 1, pp. 43–47, 2014, in Chinese.
- [24] Y. Z. Li, "Mechanical behavior on dovetail mortise-tenon joints with different pulling-out in ancient buildings," *Sichuan Building Science*, vol. 43, no. 3, pp. 1–4, 2015, in Chinese.
- [25] C. Chen, H. Qiu, and Y. Lu, "Flexural behaviour of timber dovetail mortise-tenon joints," *Construction and Building Materials*, vol. 112, pp. 366–377, 2016.
- [26] Q. F. Xie, L. P. Zhang, S. Li et al., "Cyclic behavior of Chinese ancient wooden frame with mortise-tenon joints: friction constitutive model and finite element modelling," *Journal of Wood Science*, vol. 64, no. 1, pp. 1–12, 2017.
- [27] Z. G. Wen, W. B. Hu, G. D. Qiao et al., "Research on friction energy dissipation and seismic performance of the joints of timber structures," *World Earthquake Engineering*, vol. 33, no. 1, pp. 278–283, 2017.

